Geophysical Research Letters

RESEARCH LETTER
10.1029/2018GL079813

Key Points:
- Several faults ruptured the Pacific plate seaward of Kodiak Island; most slip was on a southward-trending right-lateral strike-slip fault
- Teleseismic body waves, aftershock distribution, regional GPS offsets, and tsunami observations are used to constrain the complex faulting
- The principal stress directions are influenced by slab pull, the 1964 Alaska earthquake deformation, and collision of the Yakutat terrane

Supporting Information:
- Supporting Information S1
- Movie S1
- Movie S2

Correspondence to:
T. Lay,
tlay@ucsc.edu

Citation:
Lay, T., Ye, L., Bai, Y., Cheung, K. F., & Kanamori, H. (2018). The 2018 M_W 7.9 Gulf of Alaska earthquake: Multiple fault rupture in the Pacific plate. *Geophysical Research Letters*, *45*, 9542–9551. https://doi.org/10.1029/2018GL079813

Received 31 JUL 2018
Accepted 4 SEP 2018
Accepted article online 10 SEP 2018
Published online 22 SEP 2018

The 2018 M_W 7.9 Gulf of Alaska Earthquake: Multiple Fault Rupture in the Pacific Plate

Thorne Lay[1], Lingling Ye[2,3], Yefei Bai[4,5], Kwok Fai Cheung[5], and Hiroo Kanamori[6]

[1]Department of Earth and Planetary Sciences, University of California, Santa Cruz, CA, USA, [2]Guangdong Provincial Key Laboratory of Geodynamics and Geohazards, School of Earth Sciences and Engineering, Sun Yat-sen University, Guangzhou, China, [3]Earthquake Research Institute, University of Tokyo, Tokyo, Japan, [4]Ocean College, Zhejiang University, Zhoushan, China, [5]Department of Ocean and Resources Engineering, University of Hawai'i at Mānoa, Honolulu, HI, USA, [6]Seismological Laboratory, California Institute of Technology, Pasadena, CA, USA

Abstract A major (M_W 7.9) intraplate earthquake ruptured the Pacific plate seaward of the Alaska subduction zone near Kodiak Island on 23 January 2018. The aftershock seismicity is diffuse, with both NNW- and ENE-trending distributions, while long-period point source moment tensors have near-horizontal compressional and tensional principal strain axes and significant non-double-couple components. Backprojections from three large-aperture networks indicate sources of short-period radiation not aligned with the best double-couple fault planes. A suite of finite-fault rupture models with one to four faults was considered, and a four-fault model, dominated by right-lateral slip on an SSE trending, westward-dipping fault, is compatible with most seismic, GPS, and tsunami data. However, the precise geometry, timing, and slip distribution of the complex set of faults is not well resolved. The sequence appears to be the result of intraplate stresses influenced by slab pull, the 1964 Alaska earthquake, and collision of the Yakutat terrane in northeastern Alaska.

Plain Language Summary On 23 January 2018 a very large earthquake, with magnitude 7.8, ruptured in the Pacific plate southwest of the Alaskan subduction zone. There are multiple indications of complex faulting for this event: The point source moment tensor is not consistent with a single fault rupture; the aftershock distribution is diffuse, with nearly orthogonal trends in seismicity; the aftershock mechanisms are diverse; backprojections of short-period seismic waves show complex patterns of high-frequency energy release not on a single plane; and teleseismic waveforms are complex. Inversions of the teleseismic signals for a variety of models with from one to four different faults being allowed provide slip models that are used to predict regional GPS observations from Alaska along with deepwater tsunami recordings from seafloor pressure sensors at Deep-ocean Assessment and Reporting of Tsunamis (DART) stations. The primary rupture occurred on a fault trending SSE, dipping to the west, and several nearly perpendicular faults appear to have ruptured as well, but the limited spatial extent of the rupture makes it difficult to resolve the details of the faulting.

1. Introduction

Large subduction zone outer-rise events commonly involve shallow normal faulting and occasional deeper reverse faulting in the oceanic plate, generally attributed to plate bending stresses from slab pull that can be modulated by the interplate seismic cycle (e.g., Ammon et al., 2008; Christensen & Ruff, 1988; Dmowska et al., 1988; Lay et al., 1989). Occurrence of major intraplate earthquakes in old oceanic lithosphere seaward of subduction zone outer-rise flexure is relatively rare (Craig et al., 2014), although the largest recorded intraplate strike-slip earthquake was such an event. That was the 12 April 2012 Indo-Australian M_W 8.6 multifault rupture (e.g., Duputel et al., 2012; Hill et al., 2015; Meng et al., 2012; Wei et al., 2013; Yue et al., 2012). Another notable intraplate sequence beyond the outer rise of a subduction zone occurred in the northeastern Gulf of Alaska, when M_W 7.1 (17 November 1987), M_W 7.8 (30 November 1987), and M_W 7.7 (6 March 1988) strike-slip events struck along a north-south trend seaward of the Yakutat terrane (Figure 1; e.g., Hwang & Kanamori, 1992; Lahr et al., 1988; Pegler & Das, 1996; Quintanar et al., 1995).

On 23 January 2018 another major earthquake struck the Gulf of Alaska, initiating ~270 km southeast of Kodiak Island, Alaska, and ~90 km southeast of the Alaska trench (Figure 1). The Pacific plate has slightly right-lateral oblique convergence at ~6 cm/year near the source region. Seismic, geodetic, and tsunami

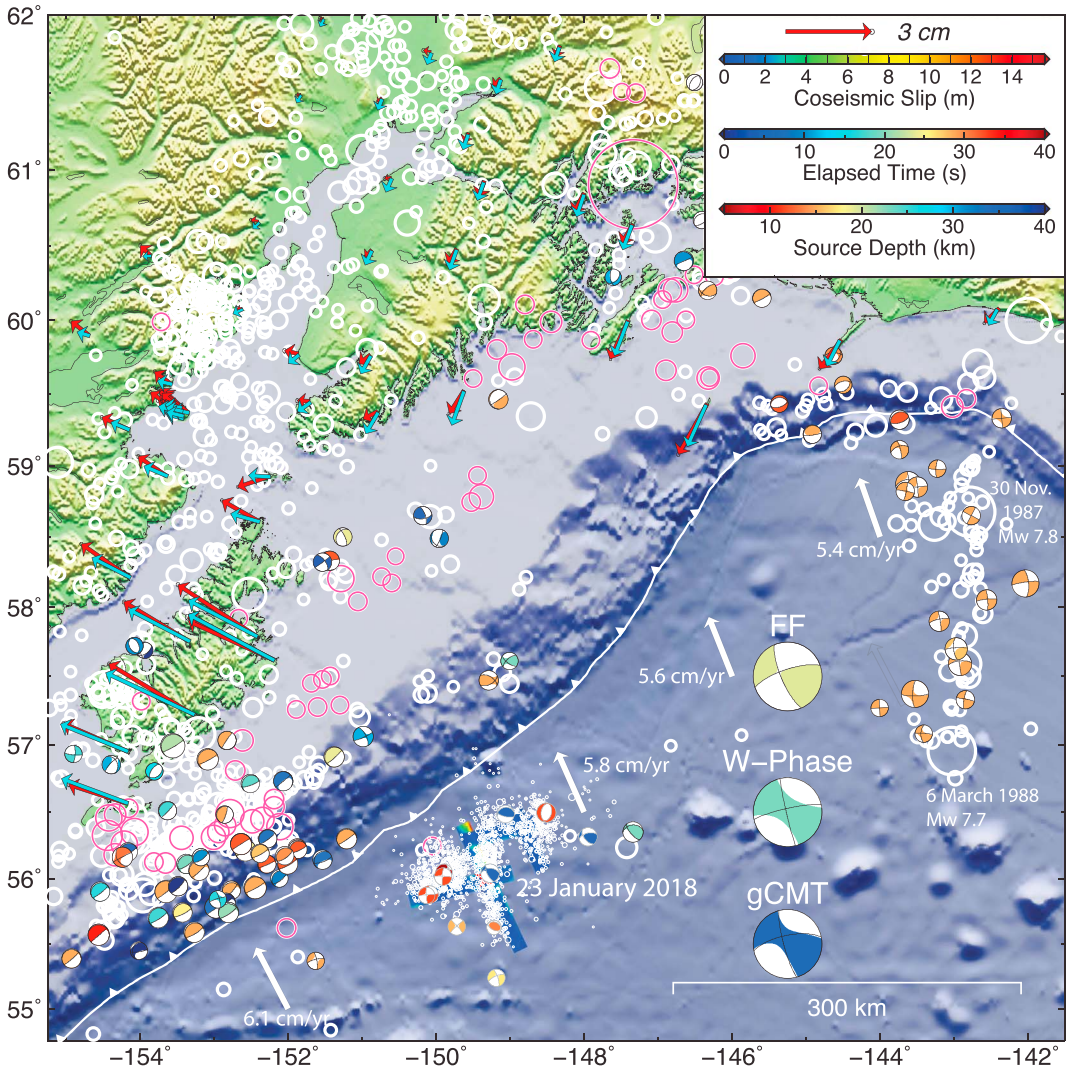

Figure 1. Regional map of the Alaska subduction zone with the incoming Pacific plate converging as indicated by the white arrows (GEODVEL: Argus et al., 2010). White circles away from the 23 January 2018 source region are NEIC locations of all events larger than magnitude 4.5 since 1900, with mainshock and first-year aftershocks for the 1964 Alaska earthquake highlighted in magenta. White circles near the source region are NEIC aftershocks larger than magnitude 2.5 through 20 February 2018. Regional focal mechanisms for events less than 30 km deep in the gCMT catalog from 1976 through 2017 are shown, color coded by source depth. Small focal mechanisms in the aftershock distribution are NEIC solutions for events through 8 February 2018. Large focal mechanisms are solutions for the 23 January 2018 event: FF = composite moment tensor from the four-fault model in this paper; *W*-phase = *W*-phase inversion described in the text; gCMT = global centroid-moment-tensor solution. Red vectors are rapid coseismic GPS displacements obtained from UNAVCO. Blue vectors are predicted GPS displacements from the four-fault source model in this paper. NEIC = National Earthquake Information Center.

observations indicate complex faulting for the 2018 event that is explored here by inversion and modeling. The strain geometry is inferred to be influenced by lateral variations in stress conditions along the Alaskan convergence zone.

2. Data and Modeling Approach

The 23 January 2018 Gulf of Alaska earthquake (09:31:40.89 UTC, 56.004°N 149.166°W, depth 14.1 km; U.S. Geological Survey National Earthquake Information Center [NEIC]: https://earthquake.usgs.gov/earthquakes/eventpage/us2000cmy3#origin) ruptured a region of very low prior seismicity (Figure 1). The global centroid-moment-tensor (gCMT) solution (http://www.globalcmt.org/CMTsearch.html) has predominantly

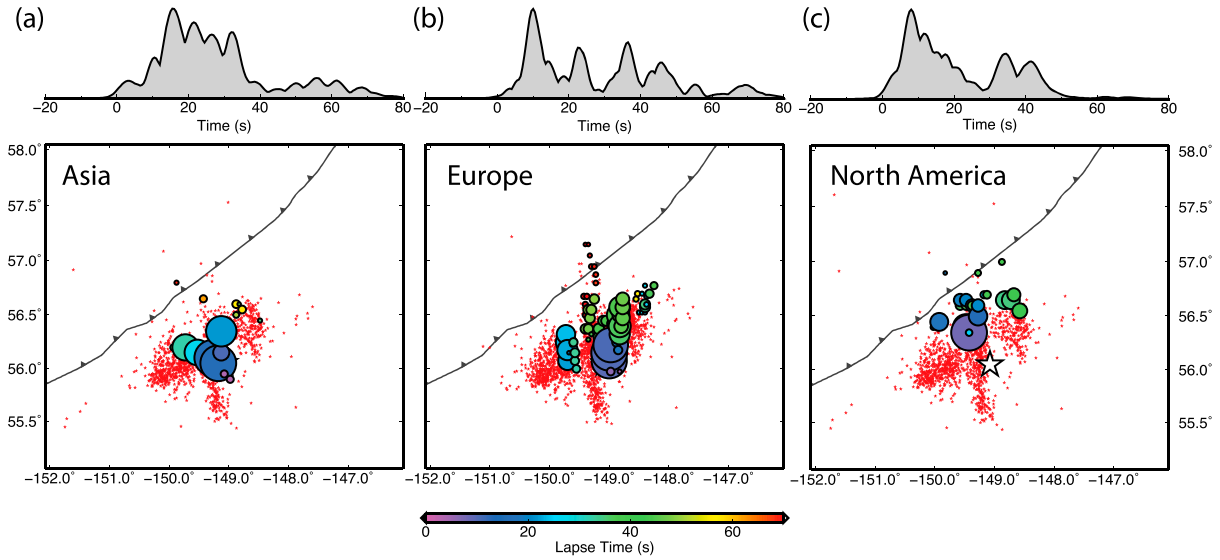

Figure 2. Back projection of high-frequency (0.5–3.0 Hz) *P* waves from broadband networks in (a) Asia, (b) Europe, and (c) North America for the 23 January 2018 Gulf of Alaska earthquake. Time-coded circles indicate loci of strong energy in the back-projected images with the time-varying peak energy for each network shown above the maps. Figure S1 shows locations, travel time shifts, and correlations with the average waveform for each network. The filtered and multistation correlation aligned waveforms are shown in Figures S2–S4. Animations of the three backprojections are shown in Movie S1. The star indicates the location of the hypocenter and the red dots are aftershocks located by the U.S. Geological Survey through 20 February 2018.

strike-slip geometry with a significant non-double-couple component (Figure 1). The seismic moment is $M_0 = 9.6 \times 10^{20}$ Nm (M_W 7.9), and the nodal planes have strike $\phi_1 = 257°$, dip $\delta_1 = 64°$, and rake $r_1 = 4°$ and $\phi_2 = 165°$, $\delta_2 = 86°$, and $r_2 = 154°$. The centroid time shift is 23.1 s, and centroid depth is 33.6 km. The NEIC centroid-moment-tensor and *W*-phase solutions are similar. We perform a *W*-phase inversion (Kanamori & Rivera, 2008) using 259 recordings from 103 stations for the passband 2–5 mHz, also obtaining a significant non-double-couple solution but a shallower centroid depth of 23.5 km. The relatively deep, but not well-constrained, long-period centroid depths indicate rupture in the lithospheric mantle, as was found for the 2012 Indo-Australian event (e.g., Duputel et al., 2012).

NEIC generated single-plane finite-fault models for the event, preferring $\phi = 258°$ and $\delta = 69°$ (https://earthquake.usgs.gov/earthquakes/eventpage/us2000cmy3#finite-fault), with a moment rate function duration ~52 s and average rupture velocity ~2 km/s. While providing a reasonable fit to teleseismic body and surface waves, the aftershock seismicity has a broad spatial distribution (Figure 1) and does not fully corroborate this specific geometry. Rather, there is a fairly strong trend in epicenters along a ~345° azimuth and ~50-km-wide north-south spread of a nearly orthogonal trench-parallel distribution. Event relocations have somewhat tightened up the distributions (e.g., Ruppert et al., 2018), but the seismicity still suggests the possibility of multiple fault plane ruptures with ill-constrained orientation. NEIC focal mechanisms for large early aftershocks include strike-slip, normal, and thrust faulting geometries (Figure 1), further complicating identification of the primary mainshock faults. The gCMT solutions for aftershocks with M_W 4.9 to 5.5 show a similar range of mechanisms, although strike-slip events dominate. The oceanic lithosphere has fracture zones that trend ~275° (Naugler & Wageman, 1973), with magnetic anomaly isochrones and flexural bending features (Reece et al., 2013) trending orthogonal to that, so neither of the best double-couple fault planes are unambiguously related to preexisting fabric in the plate.

We perform backprojection of high-frequency (0.5–3.0 Hz) *P* wave signals filtered from broadband stations in three large aperture networks in Asia (CEA stations in China, Data Management Centre of China National Seismic Network, 2007; Zheng et al., 2010), Europe, and North America (Figure S1) to infer the mainshock faulting geometry. The data are of high quality and have good regional waveform correlation (Figures S2–S4). Using the procedure of Xu et al. (2009), individual network back-projections image loci of coherent bursts of high-frequency energy, as shown in Figure 2. Moderate length strike-slip events are very difficult to reliably image with backprojection as it is unclear whether direct *P* or *sP* is being imaged, and this can lead to distinct images from different networks. In this case, the possibility of multiple simultaneous

ruptures of different planes further complicates interpretation. The images in Figure 2 share some features in common with the routine backprojections performed by Incorporated Research Institutions for Seismology (http://ds.iris.edu/spud/backprojection/16325047) and have some key similarities to each other; later loci of radiation tend to plot north of the hypocenter, with concentrations trending both northwest and northeast. The backprojection for Europe is very similar to the one shown in Ruppert et al. (2018), although they use a hypocenter further south than the NEIC location. Even allowing for complex interference that obscures the precise subevent locations, the images do not suggest rupture on any dominant plane, and the aftershock distribution extends both southward and westward to areas where no high-frequency radiation is imaged. Apparent velocities between discrete features vary from 2.8 to 3.2 km/s, but the specific features are not very coherent with each other.

Our primary data set for modeling the finite-fault characteristics of the source is comprised of teleseismic broadband *P* wave ground displacements (96 stations) and *SH* wave ground velocities (54 stations). The data have excellent azimuthal distribution and complex waveforms, for which we use the first 90 s of motion in each inversion. The *SH* observations are given half of the weight of the *P* wave observations. We use a multi-fault version of the kinematic least squares finite-fault algorithm (Hartzell & Heaton, 1983; Kikuchi & Kanamori, 1992; Ye et al., 2016), with one to four faults being assumed. Inversions are performed for prescribed fault geometries, rupture expansion velocities, and relative onset timing, with the results being compared with geodetic and tsunami observations.

The 2018 earthquake occurred fairly far offshore of the extensive geodetic network of the Plate Boundary Observatory in Alaska, so we expect limited resolution of the precise faulting geometry from static deformation. However, these data do provide an important overall constraint on the faulting. We utilize the rapid coseismic displacements determined by Tom Herring that were posted on the UNAVCO site (ftp://data-out.unavco.org/pub/products/event/pbo_180123_0932_eq44_coseis_rapid.evt). These are the red arrows in Figure 1. The data have some rapidly varying directions in close proximity measurements on Kodiak Island. The azimuthal (Φ) station coverage is one sided but shows the expected sin(2Φ) pattern for a strike-slip event. These stations are all located across the subduction zone trench and upper wedge toe relative to the source region, so detailed modeling with laterally varying media may be needed for precise inversion (e.g., Ruppert et al., 2018). Here we compute half-space displacements (Okada, 1985) for our finite-fault models to make forward predictions of the GPS data rather than including them in inversions with the teleseismic data. Our goal is to ensure that the favored models are generally compatible with the regional deformation field.

The last data set, perhaps the most sensitive to the faulting complexity and geometry, is provided by six deepwater ocean bottom pressure sensors (Figure 3). These data provide unusually good azimuthal coverage relative to the source region for the modest tsunami generated by the event. However, the predominantly strike-slip geometry results in relatively weak tsunami signals, which are hard to model confidently, as is true for other oceanic strike-slip events (e.g., Gusman et al., 2017; Lay et al., 2017). The bathymetry from the source to the deepwater sensors is relatively simple and accurately known, and the tide-corrected and filtered tsunami waveforms are simple and almost free of seismically induced oscillations compared to, for example, the signals seen on more complex bathymetry for the large 17 July 2017 strike-slip rupture in the westernmost Aleutians (Lay et al., 2017).

Our modeling of the tsunami uses the nonhydrostatic code NEOWAVE (Yamazaki et al., 2009; Yamazaki, Cheung et al., 2011), with two levels of two-way nested computational grids to capture tsunami generation and propagation for the kinematic seafloor motions from the finite-fault inversions. The level-1 grid with 1-arcmin (~1.85-km) resolution is derived from the General Bathymetry Chart of the Oceans global database (Weatherall et al., 2015) and is sufficient to resolve seamounts, the Aleutian trench, and the continental shelves across the Gulf of Alaska (Figure 3a). The level-2 grid resolves the narrow slip and deformation patches at 0.5 arcmin (~0.9 km) around the source (Figures 3b and 3c). Time steps of 0.5 and 0.2 s, respectively, are applied on the levels 1 and 2 computations to ensure model stability within a 6-hr elapsed time. Computed time series of tsunami signal are compared with sea level records at DARTs 46402, 46403, 46409, 46410, and 46419 deployed by National Oceanic and Atmospheric Administration (NOAA) and DART Endeavor operated by Ocean Networks Canada. We evaluate the predictions of GPS displacements and tsunami waveforms for each fault model and perturb the fault model parameters (geometry, timing,

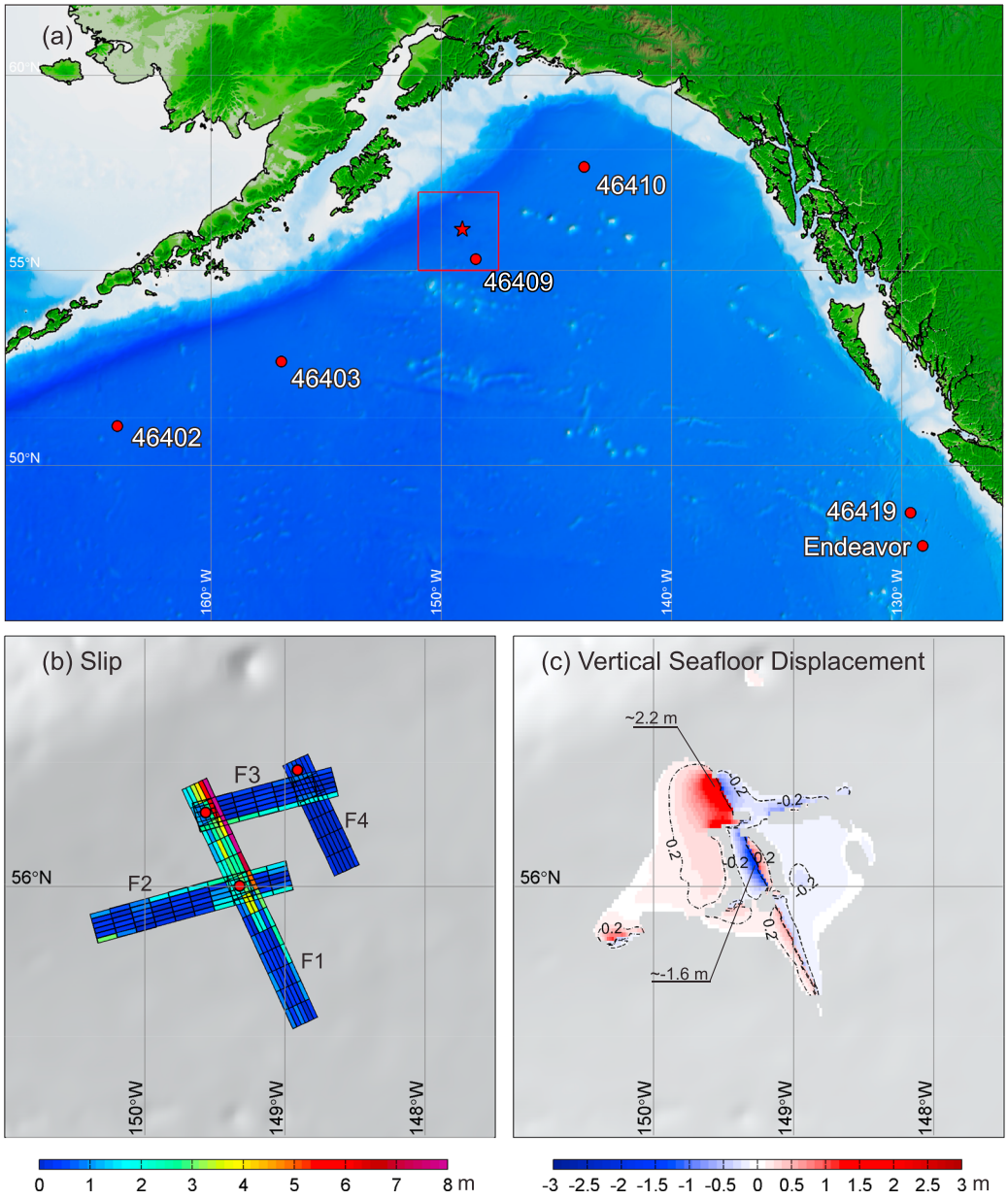

Figure 3. Computational domain setup and earthquake source for tsunami modeling. (a) Level-1 grid and position of deep-water (red dot) stations. The red rectangle indicates the source region, and the red star the hypocenter. (b) The inverted slip distribution of the four-fault (F1 to F4) model. Red dots denote the hypocenter of each fault. (c) The computed seafloor displacement of the four-fault model. The computed maximum of uplift and downdrop are specified.

and spatial placement) to iteratively strive toward a model reconciling the suite of observations, following the strategy of Yamazaki, Lay, et al. (2011) and Bai et al. (2017).

3. Rupture Models

A sequence of finite-fault models with increasing complexity is explored to match the diverse observations for the 2018 Gulf of Alaska earthquake. Similar to the NEIC modeling, long single-fault models are initially considered, utilizing nodal planes from early long-period moment-tensor solutions. Using the rapid gCMT solution nodal planes, we perform inversions for a westward-trending model with ϕ = 259° and δ = 70° (Figure S5) and a southward-trending model with ϕ = 165° and δ = 81° (Figure S6). These two models fit the teleseismic data equally well, with normalized residual waveform power of ~0.33. The hypocentral

depth is 22 km, and the fault models extend to ~45-km depth to allow for a deep centroid depth. In both cases slip is concentrated in the crustal layer, with peak slip of ~16–18 m for models having rupture expansion velocity V_r = 3 km/s.

With no clear preference provided by the teleseismic observations, we assess the solutions using tsunami observations. The westward-trending model produces poor fits to the DART buoy data other than nearby buoy 46409 (Figures 3 and S5). In contrast, the southward-trending fault model provides better fits to the waveforms at buoys 46410, 46402, and 46419 (Figures 3 and S6) but poorer fit to buoy 46409. Both models fail to match the first upswings at buoys 46403 and 46410, features that we seek to improve the fit for. This indicates the potential advantage of the tsunami waveforms for constraining the source. However, the situation is quite complex, in that due to the steeply dipping, predominantly strike-slip geometries of both faults, the seafloor deformation patterns (Figures S5b and S6b) show rapid spatial gradients in the vertical displacement that generates the tsunami. This makes the solutions sensitive to small differences in dip and rake, along with the already shorter overall tsunami wavelength than would be the case for dip-slip faulting.

Additional single-fault models with a range of strike, dip, and V_r are considered, with the prediction of GPS data in each case. The fitting of the GPS is qualitative due to the half-space modeling, but large mismatch of vector directions on Kodiak Island is used to exclude models from tsunami modeling. It is very hard to improve the fit to the tsunami for westward-trending models, and it is difficult to reduce the strong initial downswing predicted for the tsunami arrival at buoy 46410 for either fault geometry. The observed signal at 46410 is simple, with no significant bathymetric features toward the source being expected, so we sought to improve the prediction of the signal onset by considering multiple-fault models. Two-fault models, with simultaneous or staggered rupture of two planes similarly oriented to those used in the single-fault cases, were considered. A suite of teleseismic data inversions demonstrate that delaying the onset time of the westward-trending fault by 5 s or more is needed to achieve reasonable fits to the DART data (this causes the primary slip to locate on the north-south fault, which is key to fitting the DART data well). We also find that having the north-south fault dip to the east (i.e., with strike to the north) provides non-double-couple character of the composite moment tensor close to the observed long-period estimates. However, two-fault models with eastward dip produced very poor agreement with the tsunami wave polarity and waveform for models with strike ranging from 340° to 360° and dip ranging from 65° to 85°, so westward dip is preferred.

To account for the spatial spread of aftershocks and the complex trends in the backprojection images, and seeking to improve the waveform fits at stations 46403 and 46410, we next explore three- and four-fault models, placing fault segments guided by the general trends in the seismicity and backprojections. We constrained fault lengths to lie within the bounds of the cloud of aftershocks. The inversions have little sensitivity to V_r over the range 1.5 to 3.0 km/s, mainly because of uncertainty in the timing of onset of different fault ruptures (other than the need for delay of the first westward-trending fault). In all cases, the first fault to rupture has a southerly strike of from 150° to 180°, with lower values of strike providing poor fits to the seismic data. We vary the westward-trending fault strike from 245° to 260° as well. The composite mechanisms for the various fault models all tend to have small non-double-couple components when the north-south trending faults dip to the west. We consider conjugate geometries with angles between the fault sets varying from 60° to 120° and en echelon configurations of north-south faults with strike of 165° distributed across the aftershock zone, but these do not provide improvement in the DART 46410 waveform. By computing the tsunami waveforms at virtual stations around the 46410 location (Figure S7), we find that one way to reduce the initial downswing is by rotating the southward-trending strike counterclockwise to ~150°, and such rotation allowed us to simultaneously fit the waveform at 46403 better; however, the fit to the GPS stations began to degrade for strike $<$155°.

A four-fault model that fits the teleseismic, geodetic, and tsunami data quite well but does depart from the central aftershock trends by ~10° (we begrudgingly accepted this) is shown in Figures 3b and S8, with details of individual fault slip distributions given in supporting information Text S1. The primary faulting is on the southward-trending fault (F1), with ϕ = 155° and δ = 72°, with slip of up to 15.6 m in the crust and uppermost mantle. This rupture dominates the tsunami excitation. Secondary slip of 3 m is located on two almost orthogonal faults (F2 and F3) with ϕ = 255° and δ = 70°, and minor slip is located on a fault parallel to the first one (F4) offset 40 km to the east. Teleseismic waveform comparisons are shown in Figure S9, with normalized

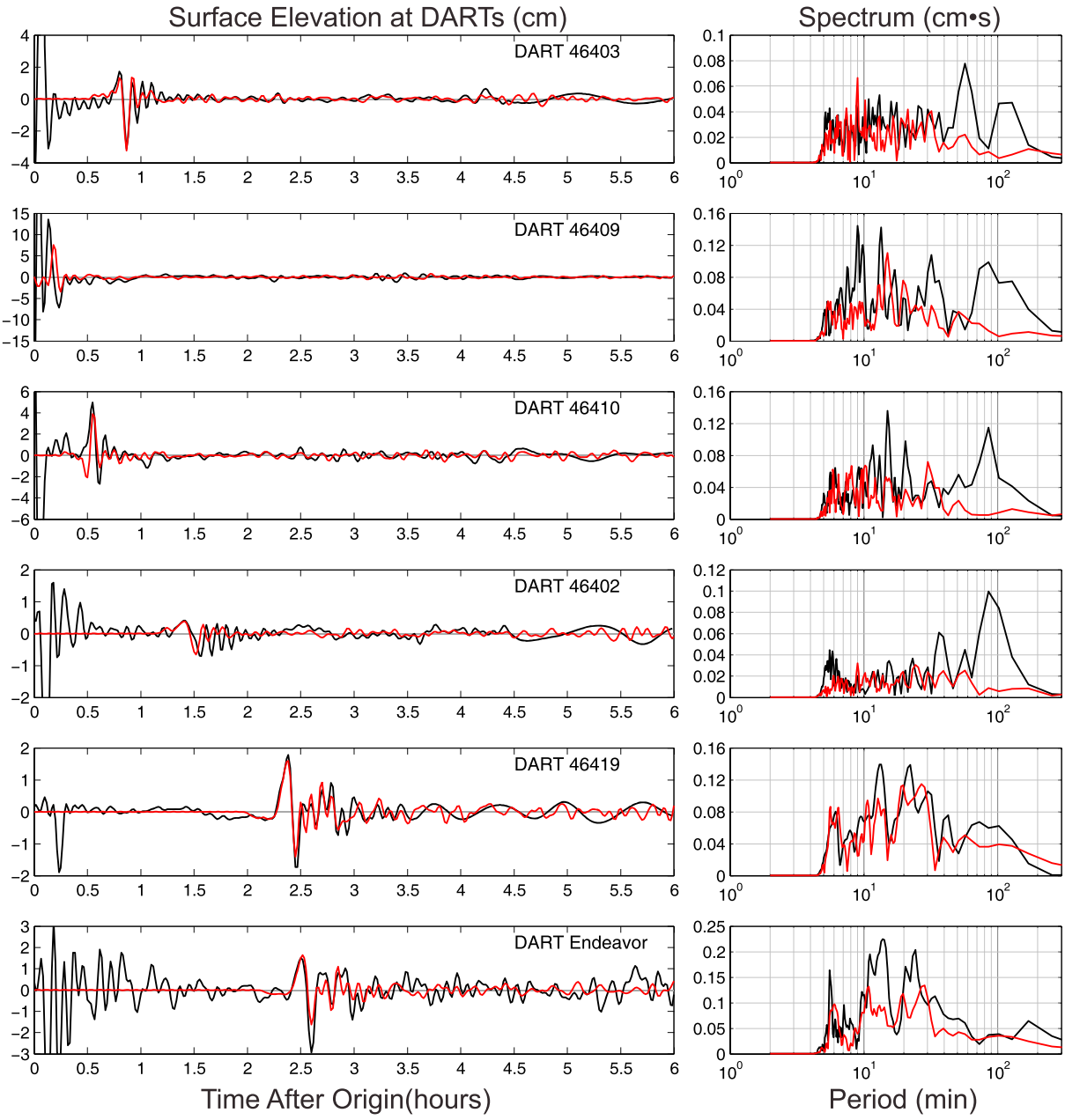

Figure 4. Comparison of water-level records (black lines) with computed waveforms and spectra (red lines) from the four-fault model. Tsunami generation and propagation are shown in Movie S2.

residual waveform misfits (~0.35) similar to many models we considered. The GPS predictions for this model are shown in Figure 1. In general, the direction and magnitude of the displacements are well matched by the half-space calculations and visually fit the data similar to inversion results in Ruppert et al. (2018). They favor a five-fault model generally similar to our model but with more slip on SW-NE faults.

Figure 3c shows the seafloor displacement for the model, and Figure 4 shows predicted tsunami waveforms at the DART stations. The predicted peak sea surface elevation for the model is shown in Figure S10. There is a diminished early downswing at 46410 and the waveform at 46403 is well fit, the first upswing and downswing at DART46419 are well matched, and the fits are generally improved relative to single-fault models shown in Figures S5 and S6, although the predicted arrival time at DART 46409 is slightly late. The fourth fault in this model produces almost no seafloor displacement (Figure 3c), and thus, it does not affect the tsunami calculation. Fitting the tsunami this well requires the primary slip to locate on the southward striking fault.

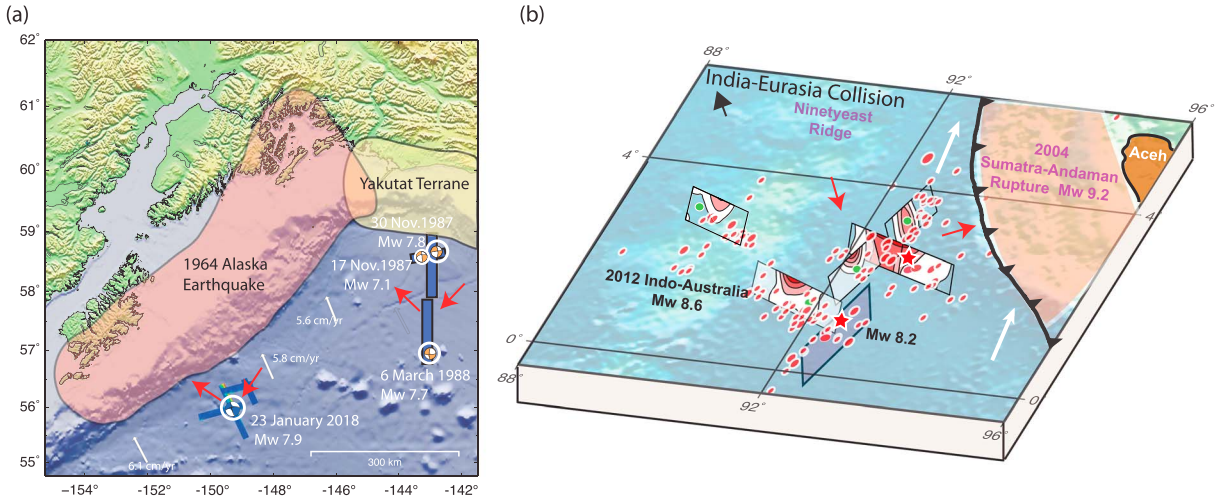

Figure 5. (a) Multiple-faulting geometries of the 1987–1988 and 2018 Gulf of Alaska earthquake sequences (rectangles) with global centroid-moment-tensor focal mechanisms on the National Earthquake Information Center epicenters. The rupture zone of the 1964 Alaska earthquake and the western portion of the colliding Yakutat terrane are shown. (b) Multiple faulting geometries for the 2012 Indo-Australian sequence. Slip zones (Yue et al., 2012) and aftershocks are indicated, along with the 2004 Sumatra-Andaman rupture zone and direction to the remote India-Eurasia collision zone. Red arrows indicate principle strain directions for the two regions, which appear to reflect both slab pull and plate boundary collisions.

With such a complex faulting model and no direct observation of seafloor deformation yet, it is difficult to evaluate the confidence level in model features. Consistent findings for the suite of models are as follows: (1) The southerly trending fault dips to the west and has large shallow slip north of and little slip south of the hypocenter, despite a southward extension of seismicity (as a result, we can rotate the southern part of the fault to lie along the seismicity trend with almost no effect on the predictions); (2) rupture on the EW plane tends to involve deeper slip and contributes to the tsunami amplitude at DART 46409; and (3) minor shallow slip northeast of the hypocenter is consistent with aftershock and backprojection features but is not well resolved. There is likely slip in the region of diffused aftershocks and backprojection features northwest of the hypocenter, but this is not resolved by the current modeling. Ruppert et al. (2018) have a fifth fault trending northward in this area, but negligible slip was put on such a fault orientation in our inversions.

4. Discussion and Conclusions

Given the notion of interplate seismic cycle modulation of the stress state in the incoming plate for strongly coupled subduction zones, the 2018 event might be expected to be affected by slab pull following the 1964 Alaska event modified by accumulating interevent compression due to relocking of that rupture zone during continued plate convergence. The tension axis for the 2018 event points landward, albeit oblique to the plate convergence direction. The compression axis for the event is directed northeast, toward the collision of the Yakutat terrane with Alaska (Reece et al., 2013) and the shallowly dipping zone of large coseismic and afterslip for the 1964 event (Suito & Freymueller, 2009), suggesting an explanation for the strike-slip faulting. There is ~10° rotation relative to the strain axes for the 1987–1988 Alaska event (Figure 5a), which are closer to the collision. The variation from India-Eurasia collision to subduction in the Sunda trench along the northern boundary of the Indo-Australian plate (Figure 5b) appears to cause the intraplate compressional and extensional principal strains to both locate near horizontal throughout the entire northern Wharton Basin (e.g., Aderhold & Abercrombie, 2016; Coblentz et al., 1998; Lay, 2018). The unusual occurrence of far outer-rise strike-slip faulting appears to require special laterally varying plate boundary conditions rather than simple two-dimensional plate bending. In both cases the primary faulting has not been located on fossil fracture zones, although secondary faulting may have been (Lay, 2018).

Analysis of teleseismic, geodetic, and tsunami observations indicates that the 23 January 2018 earthquake involves rupture of several quasi-orthogonal fault planes. The earthquake is much smaller and more

spatially compact than the great 2012 Indo-Australian earthquake, reducing directivity effects and lowering resolution of the faulting geometries, but a multifault model that accounts for many data attributes has been obtained. More detailed analysis may enhance resolution of the faulting distribution.

Acknowledgments
The Incorporated Research Institutions for Seismology (IRIS) data management service (DMS) (http://www.iris.edu/hq/) was used to access the seismic data from Global Seismic Network and Federation of Digital Seismic Network stations. Broadband data from China were obtained from the Data Management Centre of China National Seismic Network at Institute of Geophysics, Chinese Earthquake Administration (doi: 10.11998/SeisDmc/SN, http://www.seisdmc.ac.cn). GPS rapid solutions estimated by Tom Herring were accessed from the UNAVCO webpage (https://www.unavco.org). Tsunami waveform data were obtained from the NOAA National Data Buoy Center (http://www.ndbc.noaa.gov/) and Ocean Networks Canada (https://dmas.uvic.ca/). K. D. Koper kindly provided his backprojection software and training in its use. We thank editor Gavin Hayes, Jeff Freymueller, and an anonymous reviewer for helpful comments. This work was supported by NSF grant EAR1802364 to Thorne Lay and the junior Thousand Talents Plan of China and the 100 Talents program of Sun Yat-sen University to Lingling Ye.

References

Aderhold, K., & Abercrombie, R. E. (2016). Seismotectonics of a diffuse plate boundary: Observations off the Sumatra-Andaman trench. *Journal of Geophysical Research: Solid Earth*, *121*, 3462–3478. https://doi.org/10.1002/2015JB012721

Ammon, C. J., Kanamori, H., & Lay, T. (2008). A great earthquake doublet and seismic stress transfer cycle in the central Kuril islands. *Nature*, *451*(7178), 561–565. https://doi.org/10.1038/nature06521

Argus, D. F., Gordon, R. G., Heflin, M. B., Ma, C., Eanes, R. J., Willis, P., et al. (2010). The angular velocities of the plates and the velocity of the Earth's centre from space geodesy. *Geophysical Journal International*, *180*(3), 913–960. https://doi.org/10.1111/j.1365-246X.2009.04463.x

Bai, Y., Lay, T., Cheung, K. F., & Ye, L. (2017). Two regions of seafloor deformation generated the tsunami for the 13 November 2016, Kaikoura, New Zealand earthquake. *Geophysical Research Letters*, *44*, 6597–6606. https://doi.org/10.1002/2017GL073717

Christensen, D. H., & Ruff, L. J. (1988). Seismic coupling and outer rise earthquakes. *Journal of Geophysical Research*, *93*(B11), 13,421–13,444. https://doi.org/10.1029/JB093iB11p13421

Coblentz, D. D., Zhou, S., Hillis, R. R., Richardson, R. M., & Sandiford, M. (1998). Topography, boundary forces, and the Indo-Australian intra-plate stress field. *Journal of Geophysical Research*, *103*(B1), 919–931. https://doi.org/10.1029/97JB02381

Craig, T. J., Copley, A., & Jackson, J. (2014). A reassessment of outer-rise seismicity and its implications for the mechanics of oceanic lithosphere. *Geophysical Journal International*, *197*(1), 63–89. https://doi.org/10.1093/gji/ggu013

Data Management Centre of China National Seismic Network (2007). Waveform data of China National Seismic Network. Institute of Geophysics, China Earthquake Administration. https://doi.org/10.11998/SeisDmc/SN, http://www.seisdmc.ac.cn

Dmowska, R., Rice, J. R., Lovison, L. C., & Josell, D. (1988). Stress transfer and seismic phenomena in coupled subduction zones during the earthquake cycle. *Journal of Geophysical Research*, *93*(B7), 7869–7884. https://doi.org/10.1029/JB093iB07p07869

Duputel, Z., Kanamori, H., Tsai, V. C., Rivera, L., Meng, L., Ampuero, J.-P., & Stock, J. M. (2012). The 2012 Sumatra great earthquake sequence. *Earth and Planetary Science Letters*, *351-352*, 247–257. https://doi.org/10.1016/j.epsl.2012.07.017

Gusman, A. R., Satake, K., & Harada, T. (2017). Rupture process of the 2016 Wharton Basin strike-slip faulting earthquake estimated from joint inversion of teleseismic and tsunami waveforms. *Geophysical Research Letters*, *44*, 4082–4089. https://doi.org/10.1002/2017GL073611

Hartzell, S. H., & Heaton, T. H. (1983). Inversion of strong ground motion and teleseismic waveform data for the fault rupture history of the 1979 Imperial Valley, California, earthquake. *Bulletin of the Seismological Society of America*, *73*(6A), 1553–1583.

Hill, E. M., Yue, H., Barbot, S., Lay, T., Tapponnier, P., Hermawan, I., et al. (2015). The 2012 M_w 8.6 Wharton Basin sequence: A cascade of great earthquakes generated by near-orthogonal, young, oceanic-mantle faults. *Journal of Geophysical Research*, *120*, 3723–3747. https://doi.org/10.1002/2014JB011703

Hwang, L. J., & Kanamori, H. (1992). Rupture processes of the 1987-1988 Gulf of Alaska earthquake sequence. *Journal of Geophysical Research*, *97*(B13), 19,881–19,908. https://doi.org/10.1029/92JB01817

Kanamori, H., & Rivera, L. (2008). Source inversion of W phase: Speeding up seismic tsunami warning. *Geophysical Journal International*, *175*(1), 222–238. https://doi.org/10.1111/j.1365-246X.2008

Kikuchi, M., & Kanamori, H. (1992). Inversion of complex body waves—III. *Bulletin of the Seismological Society of America*, *81*(6), 2335–2350.

Lahr, J. C., Page, R. A., Stephens, C. D., & Christensen, D. H. (1988). Unusual earthquakes in the Gulf of Alaska and fragmentation of the Pacific Plate. *Geophysical Research Letters*, *18*, 1483–1486.

Lay, T. (2018). Reactivation of oceanic fracture zones in large intraplate earthquakes? In J. C. Duarte (Ed.), *Transform plate boundaries and fracture zones*. New York: Elsevier. https://doi.org/10.1016/B978-0-12-812064-4.00004-9

Lay, T., Astiz, L., Kanamori, H., & Christensen, D. H. (1989). Temporal variation of large intraplate earthquakes in coupled subduction zones. *Physics of the Earth and Planetary Interiors*, *54*(3-4), 258–312. https://doi.org/10.1016/0031-9201(89)90247-1

Lay, T., Ye, L., Bai, Y., Cheung, K. F., Kanamori, H., Freymueller, J., et al. (2017). Rupture along 400 km of the Bering fracture zone in the Komandorsky Islands earthquake (M_W 7.8) of 17 July 2017. *Geophysical Research Letters*, *44*, 12,161–12,169. https://doi.org/10.1002/2017GL076148

Meng, L., Ampuero, J.-P., Stock, J., Duputel, Z., Luo, Y., & Tsai, V. C. (2012). Earthquake in a maze: Compressional rupture branching during the 2012 M_W 8.6 Sumatra earthquake. *Science*, *337*(6095), 724–726. https://doi.org/10.1126/science.1224030

Naugler, F. P., & Wageman, J. M. (1973). Gulf of Alaska: Magnetic anomalies, fracture zones, and plate interaction. *Geological Society of America Bulletin*, *84*(5), 1575–1584. https://doi.org/10.1130/0016-7606(1973)84<1575:GOAMAF>2.0.CO;2

Okada, Y. (1985). Surface deformation due to shear and tensile faults in a half-space. *Bulletin of Seismological Society of America*, *75*(4), 1135–1154.

Pegler, G., & Das, S. (1996). The 1987-1992 Gulf of Alaska earthquakes. *Tectonophysics*, *257*(2-4), 111–136. https://doi.org/10.1016/0040-1951(95)00112-3

Quintanar, L., Madariaga, R., & Deschamps, A. (1995). The earthquake sequence of November 1987 and March 1988 in the Gulf of Alaska: A new insight. *Geophysical Research Letters*, *22*(9), 1029–1032. https://doi.org/10.1029/95GL00905

Reece, R. S., Gulick, S. P. S., Chisteson, G. L., Horton, B. K., van Avendonk, H., & Barth, G. (2013). The role of farfield tectonic stress in oceanic intraplate deformation, Gulf of Alaska. *Journal of Geophysical Research: Solid Earth*, *118*, 1862–1872. https://doi.org/10.1002/jgrb.50177

Ruppert, N. A., Rollins, C., Zhang, A., Meng, L., Holtkamp, S. G., West, M. E., & Freymueller, J. T. (2018). Complex faulting and triggered rupture during the 2018 M_W 7.9 offshore Kodiak, Alaska, earthquake. *Geophysical Research Letters*, *45*, 7533–7541. https://doi.org/10.1029/2018GL078931

Suito, H., & Freymueller, J. T. (2009). A viscoelastic and afterslip postseismic deformation model for the 1964 Alaska earthquake. *Journal of Geophysical Research*, *114*, B11404. https://doi.org/10.1029/2008JB005954

Weatherall, P., Marks, K. M., Jakobsson, M., Schmitt, T., Tani, S., Arndt, J. E., et al. (2015). A new digital bathymetric model of the world's ocean. *Earth and Space Science*, *2*(8), 331–345. https://doi.org/10.1002/2015EA000107

Wei, S., Helmberger, D., & Avouac, J.-P. (2013). Modeling the 2012 Wharton basin earthquakes off-Sumatra: Complete lithospheric failure. *Journal of Geophysical Research: Solid Earth*, *118*, 3592–3609. https://doi.org/10.1002/jgrb.50267

Xu, Y., Koper, K. D., Sufri, O., Zhu, L., & Hutko, A. R. (2009). Rupture imaging of the M_W 7.9 12 May 2008 Wenchuan earthquake from back projection of teleseismic *P* waves. *Geochemistry, Geophysics, Geosystems*, *10*, Q04006. https://doi.org/10.1029/2008GC002335

Yamazaki, Y., Cheung, K. F., & Kowalik, Z. (2011). Depth-integrated, non-hydrostatic model with grid nesting for tsunami generation, propagation, and run-up. *International Journal for Numerical Methods in Fluids*, *67*(12), 2081–2107. https://doi.org/10.1002/fld.2485

Yamazaki, Y., Kowalik, Z., & Cheung, K. F. (2009). Depth-integrated, non-hydrostatic model for wave breaking and run-up. *International Journal for Numerical Methods in Fluids*, *61*(5), 473–497. https://doi.org/10.1002/fld.1952

Yamazaki, Y., Lay, T., Cheung, K. F., Yue, H., & Kanamori, H. (2011). Modeling near-field tsunami observations to improve finite-fault slip models for the 11 March 2011 Tohoku earthquake. *Geophysical Research Letters*, *38*, L00G15. https://doi.org/10.1029/2011GL049130

Ye, L., Lay, T., Kanamori, H., & Rivera, L. (2016). Rupture characteristics of major and great ($M_W \geq 7$) megathrust earthquake from 1990-2015: 1. Moment scaling relationships. *Journal of Geophysical Research: Solid Earth*, *121*, 826–844. https://doi.org/10.1002/2015JB012426

Yue, H., Lay, T., & Koper, K. D. (2012). *En échelon* and orthogonal fault ruptures of the 11 April 2012 great intraplate earthquakes. *Nature*, *490*(7419), 245–249. https://doi.org/10.1038/nature11492

Zheng, X. F., Yao, Z. X., Liang, J. H., & Zheng, J. (2010). The role played and opportunities provided by IGP DMC of China National Seismic Network in Wenchuan earthquake disaster relief and researches. *Bulletin of the Seismological Society of America*, *100*(5B), 2866–2872. https://doi.org/10.1785/0120090257